

Article

# S-Scheme 2D/2D Heterojunction of ZnTiO<sub>3</sub> Nanosheets/Bi<sub>2</sub>WO<sub>6</sub> Nanosheets with Enhanced Photoelectrocatalytic Activity for Phenol Wastewater under Visible Light

Cheng Zuo , Xishi Tai , Zaiyong Jiang, Meifang Liu, Jinhe Jiang \*, Qian Su \* and Xueyuan Yan \* 

College of Chemistry &amp; Chemical and Environmental Engineering, Weifang University, Weifang 261000, China

\* Correspondence: 20110767@wfu.edu.cn (J.J.); sqian316@wfu.edu.cn (Q.S.); yanxueyuan@wfu.edu.cn (X.Y.)

**Abstract:** The pollution of phenol wastewater is becoming worse. In this paper, a 2D/2D nanosheet-like ZnTiO<sub>3</sub>/Bi<sub>2</sub>WO<sub>6</sub> S-Scheme heterojunction was synthesized for the first time through a two-step calcination method and a hydrothermal method. In order to improve the separation efficiency of photogenerated carriers, the S-Scheme heterojunction charge-transfer path was designed and constructed, the photoelectrocatalytic effect of the applied electric field was utilized, and the photoelectric coupling catalytic degradation performance was greatly enhanced. When the applied voltage was +0.5 V, the ZnTiO<sub>3</sub>/Bi<sub>2</sub>WO<sub>6</sub> molar ratio of 1.5:1 had highest degradation rate under visible light: the degradation rate was 93%, and the kinetic rate was 3.6 times higher than that of pure Bi<sub>2</sub>WO<sub>6</sub>. Moreover, the stability of the composite photoelectrocatalyst was excellent: the photoelectrocatalytic degradation rate of the photoelectrocatalyst remained above 90% after five cycles. In addition, through electrochemical analysis, XRD, XPS, TEM, radical trapping experiments, and valence band spectroscopy, we found that the S-scheme heterojunction was constructed between the two semiconductors, which effectively retained the redox ability of the two semiconductors. This provides new insights for the construction of a two-component direct S-scheme heterojunction as well as a feasible new solution for the treatment of phenol wastewater pollution.

**Keywords:** 2D/2D nanosheet-like ZnTiO<sub>3</sub>/Bi<sub>2</sub>WO<sub>6</sub>; S-scheme heterojunction; phenol wastewater pollution; photoelectrocatalytic degradation



**Citation:** Zuo, C.; Tai, X.; Jiang, Z.; Liu, M.; Jiang, J.; Su, Q.; Yan, X. S-Scheme 2D/2D Heterojunction of ZnTiO<sub>3</sub> Nanosheets/Bi<sub>2</sub>WO<sub>6</sub> Nanosheets with Enhanced Photoelectrocatalytic Activity for Phenol Wastewater under Visible Light. *Molecules* **2023**, *28*, 3495. <https://doi.org/10.3390/molecules28083495>

Academic Editor: Lagnamayee Mohapatra

Received: 27 March 2023

Revised: 12 April 2023

Accepted: 13 April 2023

Published: 15 April 2023



**Copyright:** © 2023 by the authors. Licensee MDPI, Basel, Switzerland. This article is an open access article distributed under the terms and conditions of the Creative Commons Attribution (CC BY) license (<https://creativecommons.org/licenses/by/4.0/>).

## 1. Introduction

With the development of the phenol industry, the pollution of phenol wastewater has become increasingly serious [1,2]. Traditional phenol wastewater treatment technology easily causes secondary pollution, which limits its application. The emerging photoelectric catalysis technology is valued by the majority of people because of its conformity to the development concept of green and environmental protection [3–5]. However, photocatalysts used in phenol wastewater have many problems. For example, TiO<sub>2</sub>, ZnO, and other materials cannot effectively use sunlight due to their wide band gap and poor response to visible light [6–8]. In addition, materials such as CdS and Cu<sub>2</sub>O are unstable due to their own chemical properties and are easily affected by light corrosion [9,10]. These reasons all limit the application of photocatalytic technology in the degradation of phenol wastewater. Therefore, it is urgent to develop new photocatalytic materials with high visible light response and stable chemical properties suitable for the degradation of phenol wastewater.

Recently, Bi<sub>2</sub>WO<sub>6</sub> has become a research focus because of its layered structure and stable properties. Studies have found that Bi<sub>2</sub>WO<sub>6</sub> has an excellent valence band structure, but the conduction band cannot reduce oxygen to superoxide radicals and the photogenerated carriers are easy to recombine, which reduces the photocatalytic efficiency [11]. For this reason, it is necessary to modify Bi<sub>2</sub>WO<sub>6</sub>. To address the problem of photogenerated

carrier transfer in traditional heterojunction and Z-scheme heterojunction photocatalysts, Fu et al. proposed the concept of S-scheme (Step-scheme) heterojunction design based on Z-scheme heterojunction without introducing electronic media (redox ion pairs or solid conductors) [12]. The S-scheme heterojunction photocatalyst consists of an oxidation scheme photocatalyst (OP) and a reduction scheme photocatalyst (RP) [13,14]. RP has a higher conduction band, valence band position, and Fermi energy level compared to OP. When RP and OP come into contact, electrons spontaneously transfer from RP to OP until the Fermi energy levels of both reach equilibrium due to the Fermi energy level difference. At this point, a great deal of electrons accumulate at the OP interface, resulting in the energy band bending downward and becoming negatively charged. As electrons are lost at the RP interface, the energy band bends upward and carries a positive charge, eventually forming a built-in electric field from RP to OP [15,16]. After illumination, OP and RP are simultaneously excited to generate photogenerated electrons. Under the synergistic effect of the internal electric field, Coulombic gravity, and band bending, the photogenerated electrons in the OP conduction band are transferred to the RP valence band. Finally, the photogenerated electrons in the RP conduction band and the photogenerated holes in the OP valence band are retained [17,18]. According to the design concept, photogenerated electrons with a weak reduction ability and photogenerated holes with a weak oxidation ability are recombined in S-scheme heterostructures. This improves the separation efficiency of photogenerated electrons and holes, retains photogenerated holes with a strong oxidation ability, and photogenerated electrons with a strong reduction ability, thereby enhancing the oxidation and reduction ability of the catalytic system [19,20].  $\text{Bi}_2\text{WO}_6$  is an excellent oxidized semiconductor due to its strong oxidation capacity of photogenic holes due to the advantage of valence band. The latest research shows that the usage of  $\text{Bi}_2\text{WO}_6$  to construct S-scheme heterojunction has an excellent effect in the photocatalytic degradation of pollutants. Li et al. designed and constructed an S-scheme  $\text{Bi}_2\text{WO}_6/\text{CoIn}_2\text{S}_4$  heterojunction, which greatly enhanced the TC degradation effect [21]. Therefore, it is still a huge challenge to directly construct a two-component S-scheme heterojunction without introducing expensive electron-mediated materials.

In addition, the latest research shows that the conduction band structure of  $\text{ZnTiO}_3$  is excellent and that the conduction band potential can reduce oxygen to superoxide radicals [22]. Researchers have used  $\text{ZnTiO}_3$  in the field of photocatalysis and have achieved certain results. Chen et al. found that the  $\text{ZnTiO}_3/\text{Zn}_2\text{Ti}_3\text{O}_8/\text{ZnO}$  ternary photocatalyst had an excellent performance in degrading organic pollutants due to its unique S-scheme heterostructure [23]. Lu et al. found that zinc titanate-based heterostructures had an enhanced photocatalytic performance [24]. The  $\text{ZnTiO}_3/\text{Zn}_2\text{Ti}_3\text{O}_8/\text{ZnO}$  heterojunction prepared via a simple phase-change method had an excellent performance in hydrogen production and water pollution treatment [25]. According to previous studies, we can see the superiority of the conduction band performance of  $\text{ZnTiO}_3$ . Therefore,  $\text{ZnTiO}_3$  is an excellent reducing semiconductor. Therefore, the recombination by coupling  $\text{ZnTiO}_3$  with a high-light electron-generating reduction ability and  $\text{Bi}_2\text{WO}_6$  with a high-light hole-generating oxidation ability at the interface to construct an S-scheme heterojunction is expected. The recombination with  $\text{ZnTiO}_3$  will definitely make up for the conduction band potential of  $\text{Bi}_2\text{WO}_6$  not forming  $\bullet\text{O}_2^-$ , and the interlacing of the two semiconductor band structures can well separate photogenerated electrons and holes. Finally, excellent results have been achieved in the degradation of phenolic pollutants.

The morphologies of the catalysts are varied. Among them, the nanosheet catalyst is more advantageous because the short electron–hole transport path reduces the loss in the transport process and the sheet structure can provide more photoactive sites for photocatalysis to promote the occurrence of the photocatalytic reaction. At present, there are no reports on the work of the S-scheme heterojunction of  $\text{ZnTiO}_3/\text{Bi}_2\text{WO}_6$  in the photocatalytic degradation of phenol wastewater. In this work, a 2D/2D nanosheet  $\text{ZnTiO}_3/\text{Bi}_2\text{WO}_6$  heterojunction system was constructed through the combination of calcining and a hydrothermal method. In addition, the photogenerated carrier was easily recombined during

the process of transferring to the catalyst surface for reaction. In order to further improve the separation efficiency of photogenerated carrier, the photoelectric coupling effect of an applied electric field was an effective strategy. The photoelectrochemical performance and photocatalytic performance of the catalyst were studied, and the electron–hole transfer mechanism and functional groups of the photocatalyst were explored. Excellent results were achieved in terms of similar pollutants. This work provides new insights for the construction of a two-component S-scheme heterojunction as well as a feasible new solution for the treatment of phenol wastewater pollution.

## 2. Results and Discussion

### 2.1. XRD Analysis

The crystal structure and crystal plane of the sample were characterized by using XRD. Figure 1 shows that the peaks at  $28.2^\circ$ ,  $32.9^\circ$ ,  $47.2^\circ$ ,  $56.0^\circ$ , and  $58.5^\circ$  corresponded to (131), (200), (220), (133), and (107) of  $\text{Bi}_2\text{WO}_6$ , respectively, according to JCPDS card No. 39-0256. On the crystal plane, compared with the standard card, there was no miscellaneous peak, indicating that the prepared  $\text{Bi}_2\text{WO}_6$  had no impurities such as  $\text{Bi}_2\text{O}_3$  or  $\text{WO}_3$  [26]. Figure 1 shows the characteristic peaks of the hexagonal phase  $\text{ZnTiO}_3$  after hydrothermal calcination. According to JCPDS card No. 39-0190, the diffraction angles of  $24.1^\circ$ ,  $32.8^\circ$ ,  $35.3^\circ$ ,  $48.8^\circ$ ,  $56.8^\circ$ ,  $63.3^\circ$ , and  $68.5^\circ$  corresponded to the (102), (104), (110), (204), (108), (300), and (208) crystal planes of  $\text{ZnTiO}_3$ , respectively. No impurity peaks such as  $\text{TiO}_2$  were found, indicating that there was no  $\text{TiO}_2$  in the prepared  $\text{ZnTiO}_3$ . The diffraction peaks after the two composites became sharp and narrow, indicating that the particle size of the composite catalyst became larger, so the stronger diffraction peaks could be attributed to the increase in the crystallinity of the composite catalyst [27]. In terms of the number of peaks, the diffraction peak of the composite catalyst corresponded to the peak of the single catalyst, indicating that the two semiconductors had successfully combined.

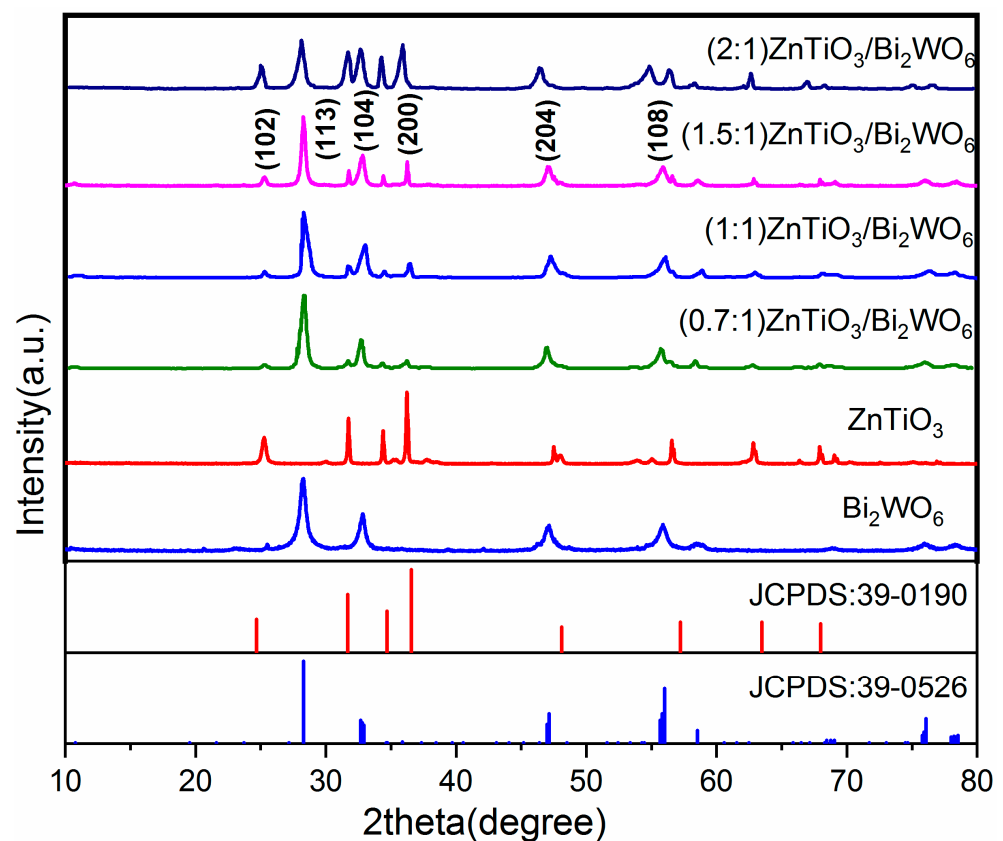
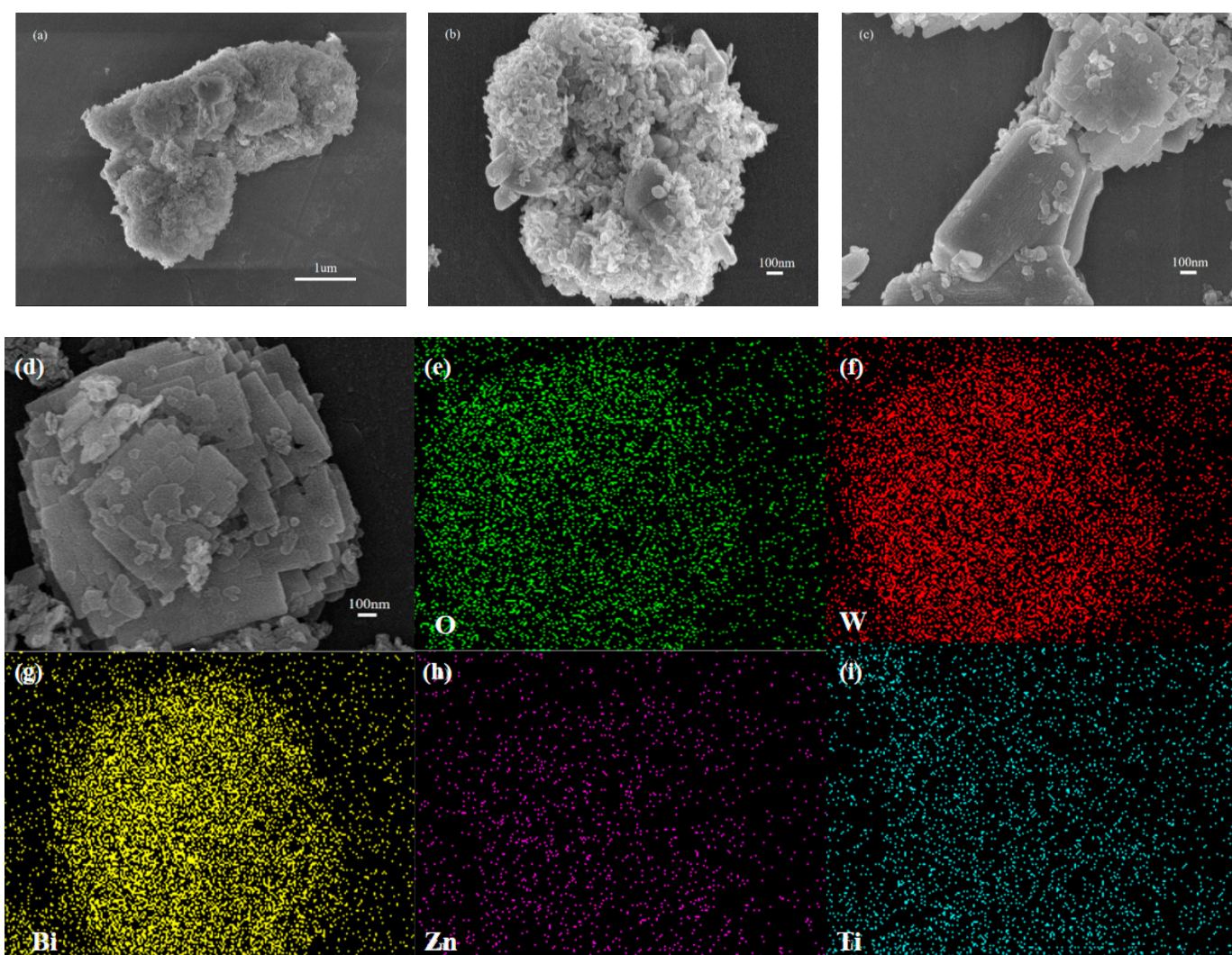


Figure 1. XRD patterns of pure  $\text{ZnTiO}_3$ , pure  $\text{Bi}_2\text{WO}_6$ , and the  $\text{ZnTiO}_3/\text{Bi}_2\text{WO}_6$  heterojunction.

## 2.2. Morphology Analysis

The morphology of the prepared catalyst can be observed in the SEM images in Figure 2. Figure 2a,b show that the  $\text{ZnTiO}_3$  was a nanosheet cluster composed of small nanosheets; Figure 2c,d show that the  $\text{ZnTiO}_3/\text{Bi}_2\text{WO}_6$  was composed of large nanosheets attached to small nanosheets. The tightly combined structure of small nanosheets and large nanosheets made the two semiconductors in the  $\text{ZnTiO}_3/\text{Bi}_2\text{WO}_6$  composite catalyst come into close contact to construct countless micro-heterojunctions and improve the utilization of visible light. Figure 2e–i show that the O, W, Bi, Zn, and Ti, respectively, were uniformly distributed, and the overall morphology of the large nanosheets of  $\text{Bi}_2\text{WO}_6$  and the cluster shape of the small nanosheets of  $\text{ZnTiO}_3$  can be observed. The larger  $\text{Bi}_2\text{WO}_6$  nanosheet and the smaller  $\text{ZnTiO}_3$  nanosheet were interleaved and in full contact with each other. The 2D nanosheets with unique morphological advantages could effectively shorten the charge-transfer path and provide a platform for the construction of heterogeneous structures. In order to determine the content of each element in the heterojunction catalyst, EDX tests were carried out; the results are shown in the inset in Figure 2d and in Table 1. The atomic ratio of O, W, Bi, Zn, and Ti was 90.12:2.92:4.93:0.62:1.41.

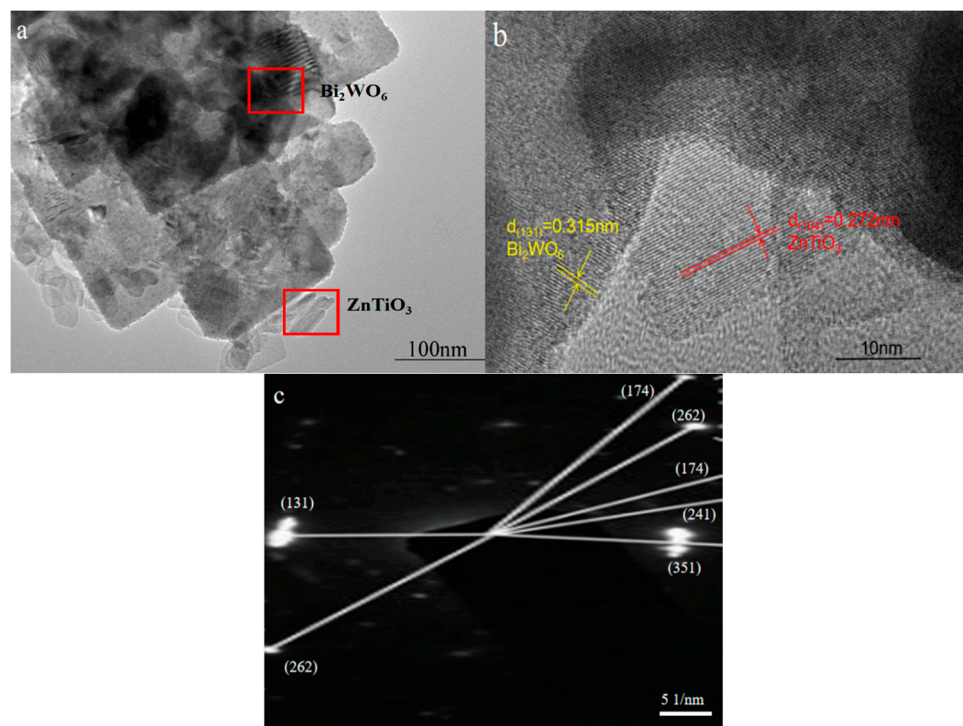


**Figure 2.** (a,b) SEM images of the  $\text{ZnTiO}_3$  sample; (c,d) SEM images of the  $\text{ZnTiO}_3/\text{Bi}_2\text{WO}_6$  heterojunction sample inset in (d): EDX of the  $\text{ZnTiO}_3/\text{Bi}_2\text{WO}_6$  heterojunction sample; and the elemental O (e), W (f), Bi (g), Zn (h), and Ti (i) mapping of the  $\text{ZnTiO}_3/\text{Bi}_2\text{WO}_6$  heterojunction sample.

**Table 1.** The content of various elements in the Bi<sub>2</sub>WO<sub>6</sub>/ZnTiO<sub>3</sub> sample according to EDX.

Element	Weight %	Atomic %
O K	46.25	90.12
Ti K	2.16	1.41
Zn K	1.30	0.62
W M	17.20	2.92
Bi M	33.09	4.93
Totals	100.00	100.00

The structure of the sample as shown in the TEM image could not only be analyzed, but the sample also could be qualitative. It can be seen in Figure 3a that the sample was composed of a large square nanosheet connected to small nanosheets, and this morphology was consistent with that observed in the SEM image. It can be seen in Figure 3b that the large nanosheet with a lattice spacing of 0.315 nm corresponded to the spacing of the Bi<sub>2</sub>WO<sub>6</sub> (131) crystal plane [28]. The small nanosheet with a lattice spacing of 0.272 nm was consistent with the (104) crystal plane of ZnTiO<sub>3</sub> [29]. It can be seen in Figure 3a,b that the connection of the two sheet-like structures could construct a heterojunction to inhibit the recombination of photogenerated carriers, and only photogenerated holes and electrons could play a redox effect to generate active groups for the photocatalytic degradation process [30]. In addition, the sheet-like structure could shorten the electron–hole transport path, which allowed holes and electrons to quickly reach the surface of the catalyst, and a redox reaction occurred with the H<sub>2</sub>O and O<sub>2</sub> attached to the surface, which activated them into the strong oxidizing free radicals •OH and •O<sub>2</sub><sup>−</sup>. At the same time, the sheet-like structure could provide a large surface area so that the organic pollutant molecules and the strong oxidizing free radicals on the surface of the catalyst were oxidized and decomposed into small inorganic molecules [31]. The SAED pattern of the synthesized heterojunction sample is shown in Figure 3c; the crystal patterns of Bi<sub>2</sub>WO<sub>6</sub> were mainly (131), (262), (174), (241), and (351). Among these, (131) was the main exposed crystal plane, which was consistent with the XRD results.

**Figure 3.** (a) TEM image, (b) HRTEM image, and (c) SAED pattern of the ZnTiO<sub>3</sub>/Bi<sub>2</sub>WO<sub>6</sub> heterojunction sample.

### 2.3. XPS Analysis

Through XPS characterization, the surface elements and valence state information of the prepared samples were understood. The distribution position of each element can be seen in Figure 4a, indicating that there were Bi, W, O, Ti, and Zn elements in the sample. It can be seen in Figure 4b that 159.05 eV and 164.38 eV corresponded to Bi4f 5/2 and Bi4f 7/2 in the Bi<sup>3+</sup> valence state, respectively, which was consistent with a previous study [32].

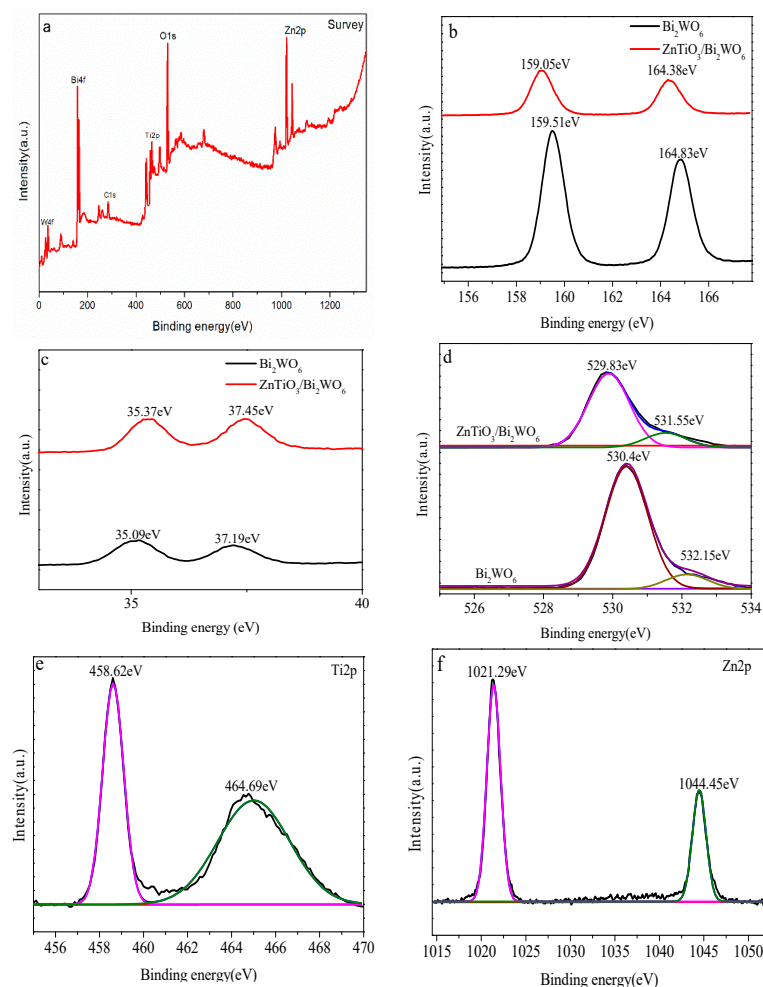


**Figure 4.** XPS spectra of pure Bi<sub>2</sub>WO<sub>6</sub> and ZnTiO<sub>3</sub>/Bi<sub>2</sub>WO<sub>6</sub> heterojunction: (a) survey spectrum; (b) Bi 4f element spectrum; (c) W 4f element spectrum; (d) O 1s element spectrum; (e) Ti 2p element spectrum; (f) Zn 2p element spectrum.

It can be seen in Figure 4c that 35.37 eV and 37.45 eV corresponded to W4f<sub>5/2</sub> and W4f<sub>7/2</sub> of the W<sup>6+</sup> valence state, respectively, which was consistent with previous studies [33,34]. In the high-resolution spectrum (Figure 4d) of the O element, the characteristic peak of O1s was decomposed into two peaks, and the binding energies of 529.83 eV and 531.55 eV corresponded to the bond energy of O1s lattice oxygen and surface hydroxyl oxygen, respectively. Two peaks could be fitted in the high-resolution spectrum (Figure 4e) of the Ti element. The binding energies of 458.6 eV and 464.5 eV corresponded to Ti2p<sub>3/2</sub> and Ti2p<sub>1/2</sub>, respectively. The difference between the two peaks was 5.9 eV, indicating that Ti in the sample was Ti<sup>4+</sup>. There were two well-fitted peaks in the high-resolution distribution (Figure 4f). The binding energies of 1021.9 eV and 1045.2 eV corresponded to Zn2p<sub>3/2</sub> and Zn2p<sub>1/2</sub>, respectively, indicating that the sample existed in the form of Zn<sup>2+</sup> [35]. It can be seen in Figure 4b–d that compared with pure Bi<sub>2</sub>WO<sub>6</sub>, the peak of the Bi element in ZnTiO<sub>3</sub>/Bi<sub>2</sub>WO<sub>6</sub> moved 0.45 eV in the direction of low binding energy, the peak of the W element of ZnTiO<sub>3</sub>/Bi<sub>2</sub>WO<sub>6</sub> moved 0.28 eV in the direction of high binding

energy, and the O element in  $\text{ZnTiO}_3/\text{Bi}_2\text{WO}_6$  moved 0.6 eV in the direction of low binding energy. The shift of binding energy in the XPS spectra was due to the construction of the S-scheme heterojunction between the two semiconductor catalysts, which led to the change in binding energy and the shift in the peak.

#### 2.4. Electrochemical Analysis

Electrochemical impedance is usually used to detect the rate of charge transfer. The smaller the radius of the arc, the smaller the resistance and the higher the separation efficiency of photogenerated carriers [36]. It can be seen in Figure 5a that the arc radius of  $\text{ZnTiO}_3/\text{Bi}_2\text{WO}_6$  was the smallest. Therefore, the impedance of  $\text{ZnTiO}_3/\text{Bi}_2\text{WO}_6$  was the lowest, the recombination of photogenerated electrons and holes was the smallest, and the photoelectric transmission performance was the best. As shown in Figure 5a, the charge-transfer resistance parameters from the EIS fitting data for the prepared catalysts was tabulated. The charge-transfer resistance parameters of  $\text{Bi}_2\text{WO}_6$ ,  $\text{ZnTiO}_3$ , and  $\text{Bi}_2\text{WO}_6/\text{ZnTiO}_3$  were 0.236 k $\Omega$ , 0.289 k $\Omega$ , and 0.158 k $\Omega$ , respectively. The curvature slope of the impedance curve in the high-frequency range of  $\text{ZnTiO}_3/\text{Bi}_2\text{WO}_6$  was greater than that of  $\text{Bi}_2\text{WO}_6$ , indicating that the composite catalyst  $\text{ZnTiO}_3/\text{Bi}_2\text{WO}_6$  had a larger capacitance and better electrochemical properties. Transient photocurrent is usually used to prove the transfer efficiency of a light-excited charge and the stability of photogenerated electrons and holes. As shown in Figure 5b, in the experiment of simulating sunlight with four switches, the photocurrent increased and stabilized instantaneously after illumination, which proved that the photogenerated charge carriers of the photocatalyst were relatively stable. The photocurrent was generated by the light-excited photocatalyst to generate electrons and air. Holes and electrons moved through the ITO glass to transmit current to produce a photocurrent curve. The photocurrent intensity of  $\text{ZnTiO}_3/\text{Bi}_2\text{WO}_6$  was 14 times and 12 times that of pure  $\text{Bi}_2\text{WO}_6$  and pure  $\text{ZnTiO}_3$ , respectively, indicating that the composite catalyst had a stronger electron transport capacity than a single catalyst, which further proved that the composite photocatalyst had a high electron–hole separation rate. This indicated that the construction of the S-scheme heterojunction accelerated the separation of charge holes and allowed more charges to work to generate a photocurrent. This result was consistent with the previous electrochemical impedance results.

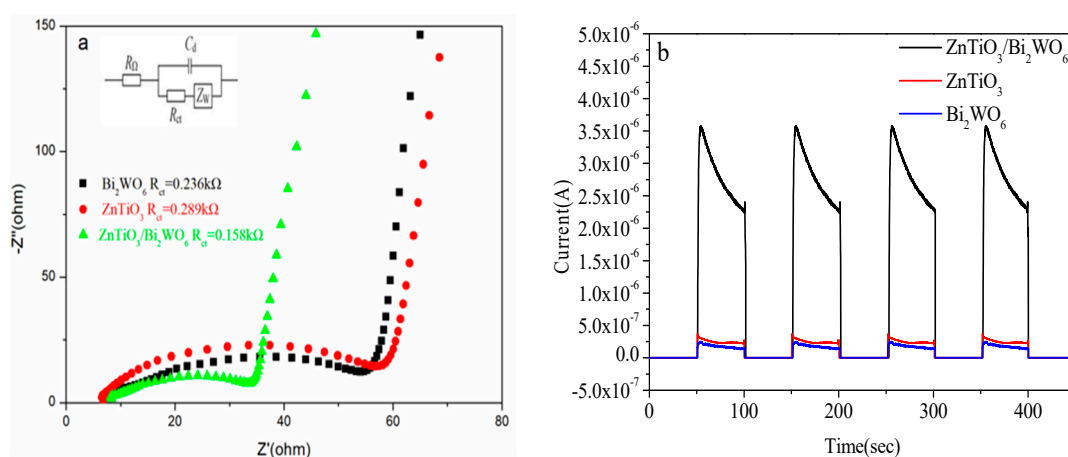


**Figure 5.** (a) Impedance spectrum of the prepared catalyst; (b) transient photocurrent curve of the prepared catalyst.

#### 2.5. Photocatalytic Degradation of Phenolic Pollutants

In order to study the performance of the prepared 2D/2D  $\text{ZnTiO}_3/\text{Bi}_2\text{WO}_6$  catalyst, a photoelectrocatalyst degradation experiment was conducted, and the results are shown in Figure 5. When the applied voltage was +0.5 V, there was no electrocatalytic degradation of all kinds of phenolic wastewater in no light, which indicated that the voltage of +0.5 V could not cause electrocatalytic degradation of phenolic wastewater. Therefore, the effect

of the applied electric field of +0.5 V was mainly photoelectric coupling, thereby promoting the effective separation of photogenerated electrons and holes. According to Figure 5a and Table 2, by comparing the degradation effects of ZnTiO<sub>3</sub>/Bi<sub>2</sub>WO<sub>6</sub> with different ratios under the same conditions, we concluded that the molar ratio of 1.5:1 had the best degradation effect; the degradation rate reached 93%. Compared with the pure-phase Bi<sub>2</sub>WO<sub>6</sub> and ZnTiO<sub>3</sub> catalysts, the degradation kinetic rate of the composite catalyst for phenol degradation increased by 3.72 times and 2.06 times, respectively. It can be seen in Figure 5b and Table 1 that the composite catalyst with a molar ratio of 1.5:1 had the largest kinetic constant. Compared with the pure Bi<sub>2</sub>WO<sub>6</sub> and ZnTiO<sub>3</sub> catalysts, the kinetics of the composite catalyst for degradation of phenol were increased by 3.6 times and 10.42 times, respectively. Compared with the literature, the photocatalytic degradation results in this paper were excellent. The results are shown in Table 3.

**Table 2.** Kinetic parameters of the prepared catalyst.

Photoelectrocatalysts	Degradation Rate	Slope	R <sup>2</sup>	Kinetic Equation
Bi <sub>2</sub> WO <sub>6</sub>	25%	0.0913	0.986	Y = 0.0913X + 0.02486
ZnTiO <sub>3</sub>	55%	0.264	0.976	Y = 0.264X – 0.07816
ZnTiO <sub>3</sub> /Bi <sub>2</sub> WO <sub>6</sub> (1:1)	77%	0.424	0.989	Y = 0.424X
ZnTiO <sub>3</sub> /Bi <sub>2</sub> WO <sub>6</sub> (1.5:1)	93%	0.9517	0.992	Y = 0.9517X – 0.195
ZnTiO <sub>3</sub> /Bi <sub>2</sub> WO <sub>6</sub> (0.7:1)	71%	0.3472	0.971	Y = 0.3472X – 0.086
ZnTiO <sub>3</sub> /Bi <sub>2</sub> WO <sub>6</sub> (2:1)	81%	0.5733	0.992	Y = 0.5733X – 0.126

Figure 6a shows the phenol degradation effect. Figure 6b shows the kinetic curves of phenol degradation for different molar ratios of ZnTiO<sub>3</sub>/Bi<sub>2</sub>WO<sub>6</sub>. According to Figure 6c–h, based on the photocatalytic experiments on p-nitrophenol, p-chlorophenol, and p-methylphenol, we found that the degradation efficiency of the photoelectrocatalyst for the methoxy electron-donating group was higher than that for the nitro electron-withdrawing group. This was because the electron-withdrawing groups such as nitro and chlorine groups could form conjugated and stable electrons with a benzene ring and the structure was stronger, and the hyperconjugation effect of electron donating groups caused the benzene ring to become strongly activated and easily reactive, so the characteristic group was easy to separate from the benzene ring, and the strong oxidizing group was more likely to attack the benzene ring and degrade phenols [37–39].

**Table 3.** Photocatalytic degradation of phenol wastewater in the presence of semiconductor nanocomposites.

Photocatalyst	Synthesis Methods	Initial Pollutant Conc.	Light Source	Degradation (%)	Ref.
Bi <sub>7</sub> O <sub>9</sub> I <sub>3</sub> /rGO	Solvothermal	10 mg/L	500 W Xe lamp (cutoff filter: λ > 420 nm)	78.3	[40]
Au/BiOBr/graphene	Hydrothermal	10 mg/L	300 W xenon lamp (cutoff filter: λ > 400 nm)	64	[41]
Silica nanosheets (SNSs)—supported mixed phase GO/SmVO <sub>4</sub>	Hydrothermal and post-annealing	20 mg/L	300 W Xe lamp with a cut-off filter	90	[42]
TiO <sub>2-x</sub> /g-C <sub>3</sub> N <sub>4</sub> nanorod arrays	Sonochemical	1.0 × 10 <sup>-4</sup> mol dm <sup>-3</sup>	35 W LED lamp	90	[43]
g-CN@CuO	Urea drop-calcined and NaBH <sub>4</sub> reduction	5 ppm	300 W Xe lamp	87	[44]
g-CN@CuO	Calcination	50 mg/L	500 W Xe lamp with a cut-off filter	87.8	[45]
ZnTiO <sub>3</sub> /Bi <sub>2</sub> WO <sub>6</sub>	Hydrothermal	10 mg/L	350 xenon lamp (λ ≥ 400 nm)	93	This work

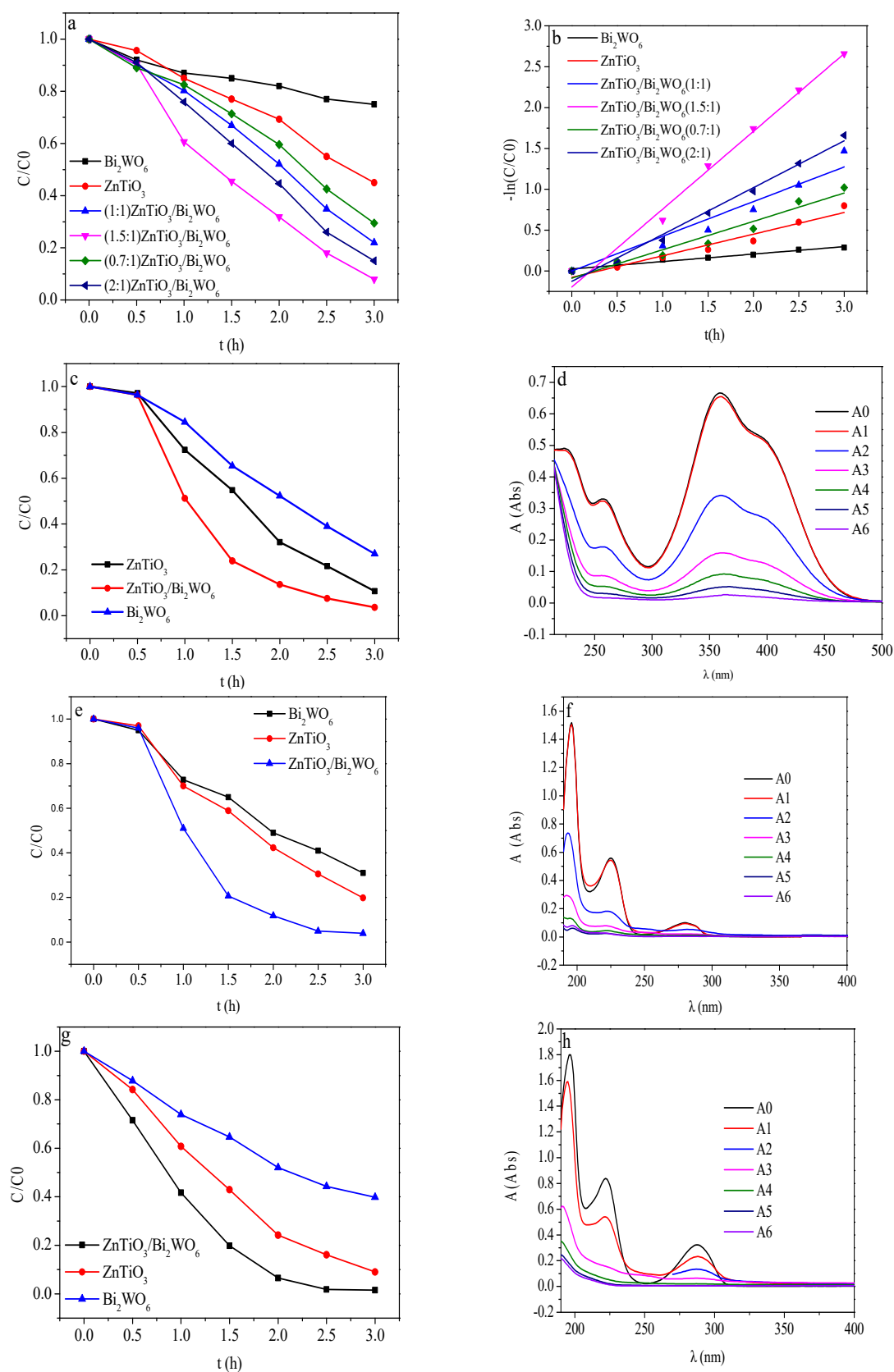


**Figure 6.** (a) Phenol degradation effect and (b) kinetic curve of phenol degradation of ZnTiO<sub>3</sub>/Bi<sub>2</sub>WO<sub>6</sub> with different molar ratios; (c) p-nitrophenol, (e) p-chlorophenol, and (g) p-methylphenol degradation effect by photocatalysts; and full-spectrum UV analysis of ZnTiO<sub>3</sub>/Bi<sub>2</sub>WO<sub>6</sub> molar ratio of 1.5:1 for (d) p-nitrophenol, (f) p-chlorophenol, and (h) p-methylphenol.

In addition, the most easily oxidized site for phenol and its derivatives was located at the ortho position to the phenolic hydroxyl group. The methyl group was located at the para position of the phenolic hydroxyl group as an electron-donating group, making the ortho position more easily oxidized. The nitro and chlorine groups as electron-withdrawing groups had a passivation effect on the benzene ring, which made the ortho position of the phenolic hydroxyl group more difficult to oxidize. The electron-withdrawing ability of nitro group was stronger than that of chlorine group, so it was more difficult to oxidize.

The stability of the photoelectrocatalytic activity of the recovered catalyst was evaluated via cyclic degradation experiments. It can be seen in Figure 7 that the stability of the composite photoelectrocatalyst was excellent. After five cycles, the photoelectrodegradation effect of the photoelectrocatalyst had hardly changed and was still maintained at more than 90%. The high stability of the photoelectrocatalyst also provided the possibility of industrialization of the photoelectrocatalytic treatment of phenolic wastewater [46].

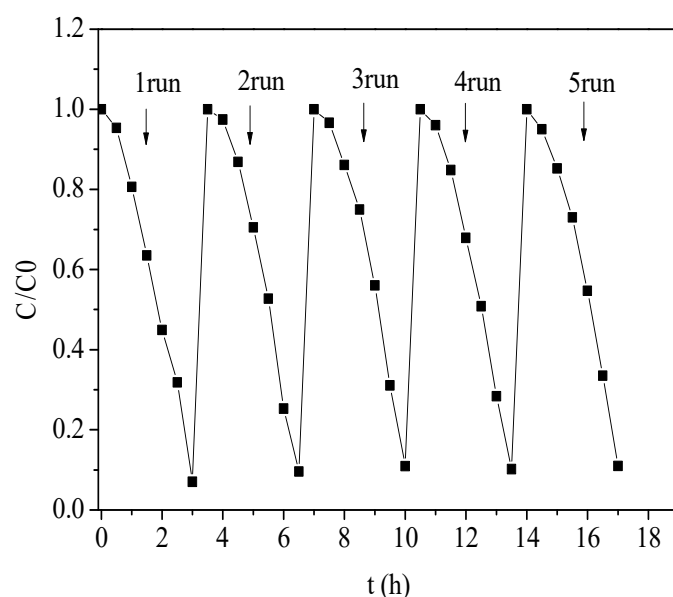
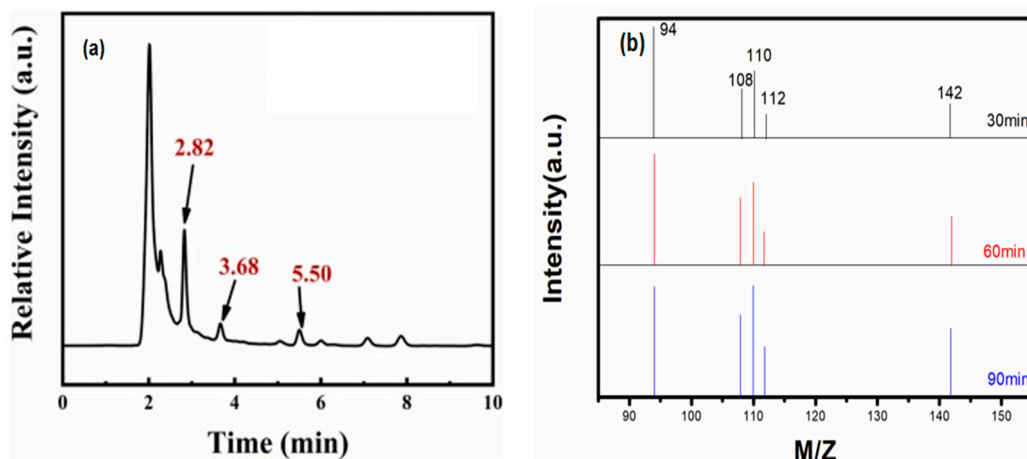


Figure 7. Cyclic stability test curve of  $\text{ZnTiO}_3/\text{Bi}_2\text{WO}_6$ .

Figure 8a shows that the phenol degradation was intermediate. In Figure 8, the HRMS has been provided for the products after 30, 60, and 90 min of degradation.  $M/Z = 94$  represents phenol;  $M/Z = 110$  represents hydroquinone, catechol, and resorcinol;  $M/Z = 108$  represents p-phenyldiquinone, o-phenyldiquinone, and m-phenyldiquinone; and  $M/Z = 142$  represents maleic acid. After the degradation of phenol, many organic products were produced, among which the main intermediate products were hydroquinone, p-benzoquinone, and maleic acid. The content of maleic acid increased with the longer degradation time. These results indicated that the main path of photocatalytic degradation of phenol was phenol  $\rightarrow$  hydroquinone  $\rightarrow$  p-benzoquinone  $\rightarrow$  maleic acid.

## 2.6. Possible Photoelectrocatalytic Mechanism

The photoelectrocatalytic mechanism of  $\text{ZnTiO}_3/\text{Bi}_2\text{WO}_6$  under visible light with the applied voltage of +0.5 V was worth pondering. In order to study the mechanism of  $\text{ZnTiO}_3/\text{Bi}_2\text{WO}_6$ , free radical-trapping experiments were carried out. We captured  $\bullet\text{OH}$  with isopropanol (IPA),  $\text{h}^+$  with ammonium oxalate (AO),  $\bullet\text{O}_2^-$  with 1,4-benzoquinone (BQ), and  $\text{e}^-$  with  $\text{AgNO}_3$ . The concentration of IPA, TEOA, BQ, and  $\text{AgNO}_3$  was 1 mM. As shown in Figure 9a,b, after adding BQ and AO, the photocatalytic efficiency decreased from 93% to 7% and 17%, respectively, which indicated that  $\bullet\text{O}_2^-$  and  $\text{h}^+$  were the main active groups. After adding IPA, the photocatalytic efficiency dropped from 93% to 27%, indicating that  $\bullet\text{OH}$  was the secondary active group.



**Figure 8.** (a) Intermediates of phenol degradation and (b) mass-to-charge ratio of products after 30, 60, and 90 min of degradation as identified by GC-MS.

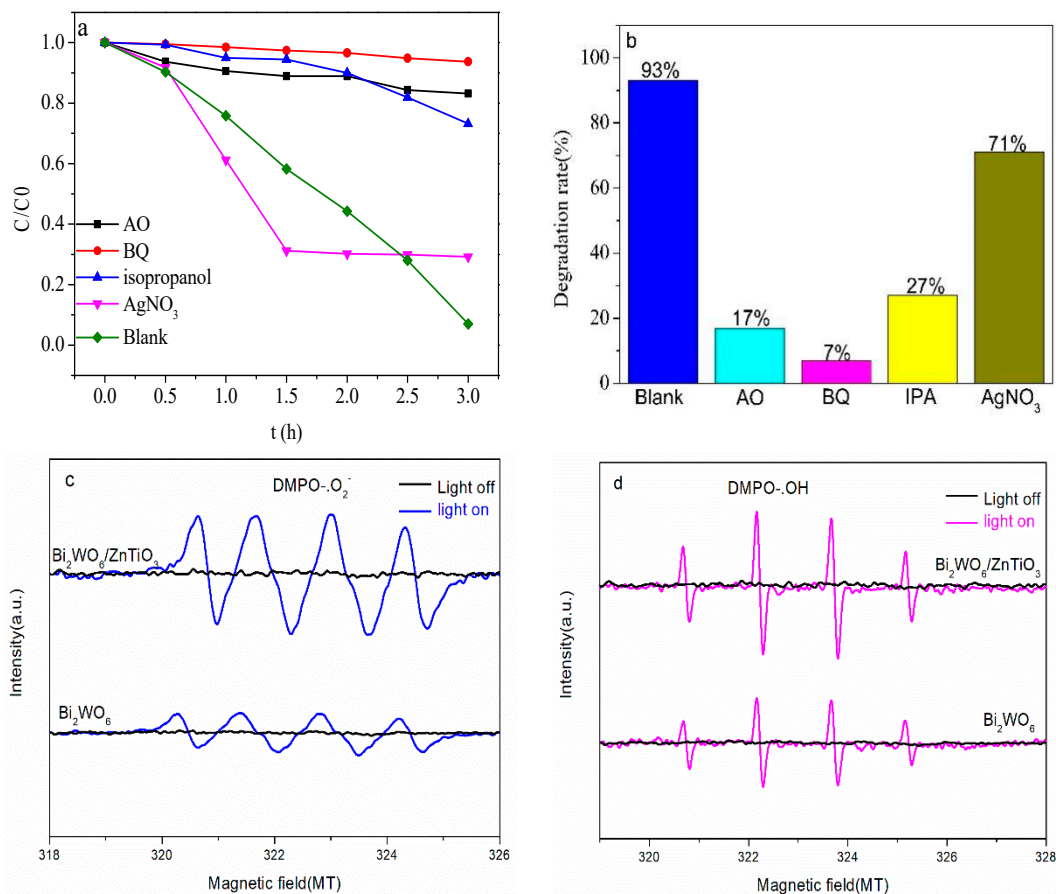


**Figure 9.** Effect of quencher on phenol degradation rate. (a) Degradation curve diagram, (b) histogram of degradation rate, (c) DMPO- $\text{O}_2^-$ , and (d) DMPO- $\text{OH}$  spin-trapping ESR spectra for  $\text{Bi}_2\text{WO}_6$  and  $\text{Bi}_2\text{WO}_6/\text{ZnTiO}_3$ .

After adding  $\text{AgNO}_3$ , the photoelectrocatalytic efficiency dropped from 93% to 71%, indicating that  $e^-$  mainly played a supplementary role and was not an active group. After  $\text{AgNO}_3$  was added,  $\text{Ag}^+$  combined with  $e^-$  to generate Ag nanoparticles under light conditions, which quenched  $e^-$ . The generated Ag nanoparticles promoted photogenerated electrons and holes due to the local surface plasmon resonance effect when the Ag content was low, which was beneficial to the degradation of phenol, so before 1.5 h, the degradation effect of phenol was better than that of blank. After 1.5 h, the content of Ag nanoparticles

was higher than that of the generated Ag nanoparticles, and Ag nanoparticles became new recombination centers of photogenerated electrons and holes, which greatly reduced the degradation effect of phenol.

In addition, it can be seen in the ESR spectra in Figure 9c,d that for  $\text{Bi}_2\text{WO}_6/\text{ZnTiO}_3$ , the signal of  $\cdot\text{OH}$  and the signal of  $\cdot\text{O}_2^-$  were obviously enhanced, which was consistent with the results of the free radical-capture experiment. This fully proved that the photogenerated carrier separation efficiency of  $\text{Bi}_2\text{WO}_6/\text{ZnTiO}_3$  was significantly improved. The performance of PEC to degrade phenolic wastewater was improved, which was mainly due to the accumulation of  $\text{h}^+$  and  $\cdot\text{OH}$  in the valence band of  $\text{Bi}_2\text{WO}_6$  and  $\text{e}^-$  and  $\cdot\text{O}_2^-$  in the conduction band of  $\text{ZnTiO}_3$ . This also indirectly proved the structure of the S-scheme heterojunction in  $\text{Bi}_2\text{WO}_6/\text{ZnTiO}_3$ .

In order to determine the band gap, valence band position, photogenerated carrier separation efficiency, and Fermi level of  $\text{Bi}_2\text{WO}_6$ ,  $\text{ZnTiO}_3$ , and  $\text{Bi}_2\text{WO}_6/\text{ZnTiO}_3$ , UV-vis spectroscopy, valence band XPS, PL, and work function tests were performed. The results is shown in Figure 10. According to Figure 10a, the visible light absorption capacity of  $\text{Bi}_2\text{WO}_6/\text{ZnTiO}_3$  after composition was obviously enhanced. Figure 8b shows that the bandgaps of  $\text{Bi}_2\text{WO}_6$ ,  $\text{ZnTiO}_3$ , and  $\text{Bi}_2\text{WO}_6/\text{ZnTiO}_3$  were 2.71 eV, 2.80 eV, and 2.58 eV, respectively. Figure 10c shows the valence band positions of  $\text{Bi}_2\text{WO}_6$  and  $\text{ZnTiO}_3$  at 3.19 eV and 2.15 eV, respectively. Figure 10d shows that the PL spectral signal of  $\text{Bi}_2\text{WO}_6/\text{ZnTiO}_3$  after composition was significantly weakened and that there was no obvious absorption peak, which indicated that the separation efficiency of the photogenerated carrier was significantly improved. The charge-transfer mechanism at the interface of  $\text{Bi}_2\text{WO}_6/\text{ZnTiO}_3$  after recombination may have been the S-scheme heterojunction.

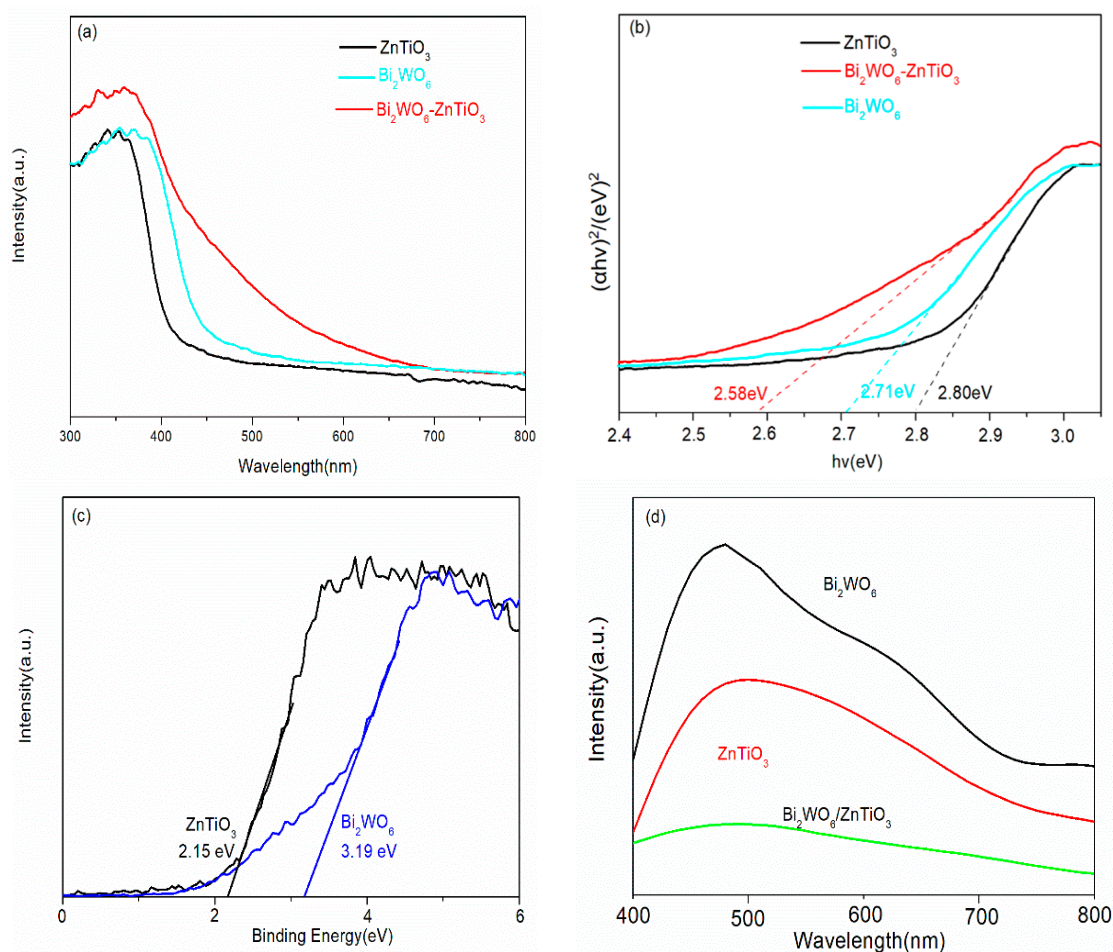
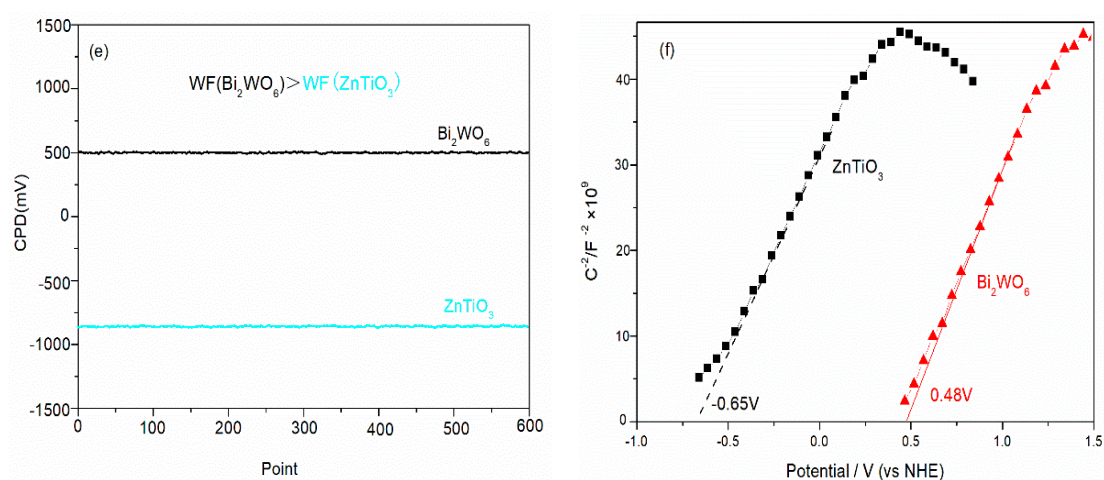


Figure 10. Cont.



**Figure 10.** (a) UV–vis spectroscopy, (b) band gap, (c) valence band position, (d) PL spectroscopy, and (e) work function of the  $\text{Bi}_2\text{WO}_6$ ,  $\text{ZnTiO}_3$ , and  $\text{Bi}_2\text{WO}_6/\text{ZnTiO}_3$  catalysts; and (f) the flat band potentials according to a Mott–Schottky electrochemistry spectroscopy test.

In order to determine the transport direction of photogenerated electrons and holes in the  $\text{Bi}_2\text{WO}_6/\text{ZnTiO}_3$  catalysts, the work functions of  $\text{Bi}_2\text{WO}_6$  and  $\text{ZnTiO}_3$  were measured using a Kelvin probe system (SKP5050, KP Technology Ltd.). The formula was as follows:  $\text{WF}(\text{Sample}) = \text{WF}(\text{tip}) + \text{CPD}$ . Calibration of the WF (tip) was realized with a standard gold sheet (gold, 5.10 eV). CPD was the contact potential difference between the sample and the tip (gold, 5.10 eV). The results are shown in Figure 10e. The work function of  $\text{Bi}_2\text{WO}_6$  was 5.60 eV and that of  $\text{ZnTiO}_3$  was 4.25 eV. Therefore, the Fermi energy level of the work function of  $\text{Bi}_2\text{WO}_6$  was significantly lower than that of  $\text{ZnTiO}_3$ . When  $\text{ZnTiO}_3$  was in contact with  $\text{Bi}_2\text{WO}_6$ , photogenerated electrons transferred from the conduction band of  $\text{Bi}_2\text{WO}_6$  to the valence band of  $\text{ZnTiO}_3$  for quenching. In addition, the flat band potentials of the photocatalysts is reported according to the Mott–Schottky test. As shown in Figure 10f, the flat band potential of  $\text{ZnTiO}_3$  was  $-0.65$  V, and the flat band potential of  $\text{Bi}_2\text{WO}_6$  was 0.48 V. Photogenerated holes accumulated in the valence band of  $\text{Bi}_2\text{WO}_6$  with a stronger oxidation capacity, and photogenerated electrons accumulated in the conduction band of  $\text{ZnTiO}_3$  with a stronger reduction capacity, forming an S-scheme heterojunction charge-transfer mechanism at the interface.

According to the experimental and characterization results, Figure 11 shows the electron–hole transfer pathway and the photoelectrocatalytic mechanism on the  $\text{ZnTiO}_3/\text{Bi}_2\text{WO}_6$  heterojunction. Under visible light irradiation, electrons were excited from the valence band (VB) of  $\text{Bi}_2\text{WO}_6$  and  $\text{ZnTiO}_3$  to the conduction band (CB). Assuming the photocatalytic mechanism was as shown in Figure 11a, because the VB position of  $\text{Bi}_2\text{WO}_6$  was higher than the HOMO position of  $\text{ZnTiO}_3$ , the valence band holes of  $\text{Bi}_2\text{WO}_6$  were transferred to the valence band of  $\text{ZnTiO}_3$  because the CB position of  $\text{Bi}_2\text{WO}_6$  was lower than the LUMO position of  $\text{ZnTiO}_3$ . The electrons were transferred to the conduction band of  $\text{Bi}_2\text{WO}_6$  [47]. However, because the HOMO potential of  $\text{ZnTiO}_3$  (2.15 eV) was less than  $E(\text{H}_2\text{O}/\bullet\text{OH})$  (2.38 eV), the amount of holes in the HOMO of  $\text{ZnTiO}_3$  was not enough to oxidize  $\text{H}_2\text{O}$  to  $\bullet\text{OH}$  radicals. Therefore, through the reaction, the holes of  $\text{ZnTiO}_3$  could not form  $\bullet\text{OH}$  radicals [48]. Since the conduction band potential of  $\text{Bi}_2\text{WO}_6$  was more positive than the standard redox potential of  $E(\text{O}_2/\bullet\text{O}_2^-)$  ( $-0.33$  eV), superoxide radical groups could not be formed, which was inconsistent with the conclusion drawn from the quencher experiment [49]. Assuming that according to the photocatalytic mechanism shown in Figure 8b, the holes of  $\text{ZnTiO}_3$  were combined with the electrons of  $\text{Bi}_2\text{WO}_6$ , only the holes of  $\text{Bi}_2\text{WO}_6$  and the electrons of  $\text{ZnTiO}_3$  were retained. Because the lowest unoccupied molecular orbital (LUMO) position of  $\text{ZnTiO}_3$  was more than  $E(\text{O}_2/\bullet\text{O}_2^-)$  ( $-0.33$  eV), the standard redox potential was more negative [50,51]. Therefore, the photoelectrons in  $\text{ZnTiO}_3$  could easily reduce the  $\text{O}_2$  adsorbed on the catalyst surface to generate  $\bullet\text{O}_2^-$  radicals because

the VB position of  $\text{Bi}_2\text{WO}_6$  (3.19 eV) was more correct than the standard redox potentials  $E(\text{OH}^-/\cdot\text{OH})$  (1.99 eV) and  $E(\text{H}_2\text{O}/\cdot\text{OH})$  (2.38 eV). The holes in the VB of  $\text{Bi}_2\text{WO}_6$  reacted with water or  $\text{OH}^-$  in water to form  $\cdot\text{OH}$ ,  $\cdot\text{OH}$ , and  $\cdot\text{O}_2^-$  radicals, which oxidatively degraded the phenolic macromolecules into small molecular products. This derivation was consistent with the conclusions of the quencher experiment, so the most likely explanation is that the  $\text{ZnTiO}_3/\text{Bi}_2\text{WO}_6$  heterojunction was a direct S-scheme photoelectrocatalytic mechanism. In the direct S-scheme semiconductor, the heterojunction formed by the two semiconductors not only retained the superior oxidation–reduction potential, but also reduced the recombination rate of photogenerated electron–hole pairs. This solution greatly improved the oxidation–reduction ability of the  $\text{Bi}_2\text{WO}_6$  photoelectrocatalysis.

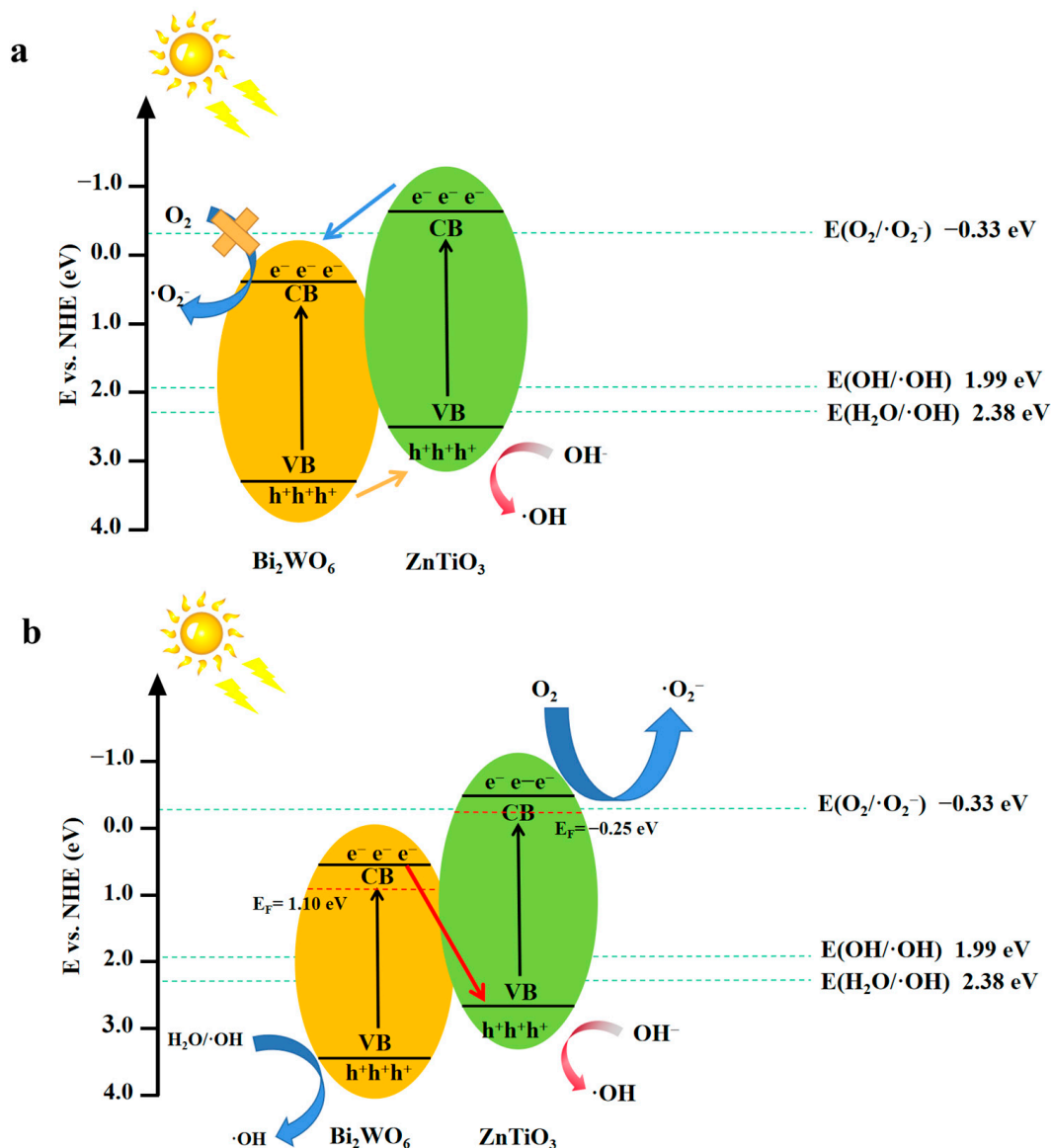


**Figure 11.** (a) P-n heterojunction and (b) S-scheme heterojunction mechanism of  $\text{ZnTiO}_3/\text{Bi}_2\text{WO}_6$ .

### 3. Experiments

#### 3.1. Materials

$\text{Zn}(\text{CH}_3\text{COO})_2$  (AR) (99%),  $\text{Bi}(\text{NO}_3)_3 \cdot 5\text{H}_2\text{O}$  (AR) (99.999%),  $\text{Ti}(\text{OC}_4\text{H}_9)_4$  (AR) (99%), and  $\text{Na}_2\text{WO}_4 \cdot 2\text{H}_2\text{O}$  (AR) (99.99%) were purchased from China Sinopharm Chemical Reagent Co. Ltd., Shanghai, China; ethanol (AR),  $\text{CO}(\text{NH}_2)_2$  (AR) (99.99%),  $\text{Na}_2\text{SO}_4$  (AR) (99.99%), and ethylene glycol (AR) (99.99%) were purchased from Tianjin Kemiou Chemical

Reagent Company, Tianjin, China; and the deionized water was made in the laboratory.

### 3.2. Preparation of $\text{Bi}_2\text{WO}_6$ and $\text{ZnTiO}_3$

First, 2 mmol of  $\text{Bi}(\text{NO}_3)_3 \cdot 5\text{H}_2\text{O}$  and 1 mmol of  $\text{Na}_2\text{WO}_4 \cdot 2\text{H}_2\text{O}$  were added to 30 mL of ethylene glycol and ultrasonically dispersed for 10 min. The resulting  $\text{Na}_2\text{WO}_4 \cdot 2\text{H}_2\text{O}$  solution was slowly added dropwise to the  $\text{Bi}(\text{NO}_3)_3 \cdot 5\text{H}_2\text{O}$  solution and then ultrasonically dispersed for 30 min so the solution was mixed thoroughly. Then, the mixed solution was poured into a 100 mL solvothermal reactor and placed in an oven at  $160\text{ }^\circ\text{C}$  for heating for 12 h. The prepared product was centrifuged. The lower solid was washed with ethanol and deionized water and dried in a vacuum drying oven at a temperature of  $60\text{ }^\circ\text{C}$  for 24 h to obtain the prepared  $\text{Bi}_2\text{WO}_6$  powder.

The  $\text{ZnTiO}_3$  with a cluster nanoflake structure was successfully prepared by using a two-step calcination method. First, 8.62 g of  $\text{Zn}(\text{CH}_3\text{COO})_2$  and 9.86 g of  $\text{Ti}(\text{OC}_4\text{H}_9)_4$  were dissolved in a 100 mL ethanol solution of 1 mol/L of urea and stirred evenly, and the solution was poured into 200 mL of solvent. The reaction kettle was placed in an oven at  $160\text{ }^\circ\text{C}$  and heated for 12 h; the molar ratio of the Zn:Ti elements was (1:1). After washing and drying the obtained  $\text{ZnTiO}_3$  precursor, it was placed into a muffle furnace and calcined at  $700\text{ }^\circ$  for 3 h and then subjected to secondary heat treatment and calcined at  $800\text{ }^\circ$  for 5 h to obtain a pure  $\text{ZnTiO}_3$  powder.

### 3.3. Preparation of $\text{ZnTiO}_3/\text{Bi}_2\text{WO}_6$

The  $\text{ZnTiO}_3/\text{Bi}_2\text{WO}_6$  composite photocatalyst was prepared by using a hydrothermal method. First, 2 mmol of  $\text{Bi}(\text{NO}_3)_3 \cdot 5\text{H}_2\text{O}$  and 1 mmol of  $\text{Na}_2\text{WO}_4 \cdot 2\text{H}_2\text{O}$  were each added to 30 mL of deionized water and stirred for 10 min. Then, the  $\text{Na}_2\text{WO}_4 \cdot 2\text{H}_2\text{O}$  solution was slowly added dropwise to the  $\text{Bi}(\text{NO}_3)_3 \cdot 5\text{H}_2\text{O}$  solution. This mixed solution was called solution A. The pH of solution A was adjusted to 7 with 0.1 mol/L of NaOH solution and stirred for 30 min. According to the different molar ratio of Zn:Bi, the  $\text{ZnTiO}_3$  prepared above was added to 10 mL of deionized water and ultrasonicated for 30 min to make the dispersion uniform. This ultrasonic suspension, which was called solution B, was added to solution A, and the mixed solution was transferred to a 100 mL hydrothermal reactor and kept at  $160\text{ }^\circ\text{C}$  for 12 h. Then, the prepared product was centrifuged. The lower solid was washed with ethanol and deionized water and dried in a vacuum drying oven at  $60\text{ }^\circ\text{C}$  for 24 h to obtain  $\text{ZnTiO}_3/\text{Bi}_2\text{WO}_6$  photocatalysts with different molar ratios.

### 3.4. Photoelectrocatalytic Degradation of Phenolic Pollutants

First, 100 mL of 10 mg/L phenol solution, 100 mL of 10 mg/L p-nitrophenol solution, 100 mL of 10 mg/L p-chlorophenol solution, and 100 mL of 10 mg/L 4-methylphenol solution were each selected as a pollutant. The photoelectrocatalytic degradation was carried out with a CHI660E three-electrode system electrochemical workstation. An Ag/AgCl electrode was used as the reference electrode, a Pt electrode was used as the counter electrode, and the photocatalyst-coated ITO conductive glass was used as the working electrode. The preparation process was to first mix 10 mg of catalyst and 5 mL of ethanol solution. The mixed system was ground for 15 min, then a proper amount of supernatant was added to ethanol and diluted for 5 min to uniformity, spin-coated on ITO glass, and dried at  $60\text{ }^\circ\text{C}$ . The light source was 350 W xenon lamp ( $\lambda \geq 400\text{ nm}$ ), the electrolyte solution was a 0.1 mol/L  $\text{Na}_2\text{SO}_4$  solution, and the applied voltage was +0.5 V. Then, photocatalyst-coated ITO and 100 mL of 10 mg/L phenolic pollutant solution was dispersed for 30 min to reach the equilibrium of adsorption and desorption of organic pollutants in the dark. We took 4 mL samples every 30 min under the illumination of the 350 W xenon lamp ( $\lambda \geq 400\text{ nm}$ ) to centrifuge and separate the supernatant. We calculated the degradation rate as  $D = (1 - C_t/C_0) \times 100\%$ . In the above formula,  $C_0$  is the concentration of the phenolic solution before degradation,  $C_t$  is the concentration of the phenolic solution after different degradation times, and D is the calculated degradation rate.

### 3.5. Electrochemical Analysis

The electrochemical analysis was carried out with a CHI660E three-electrode system electrochemical workstation. An Ag/AgCl electrode was used as the reference electrode, a Pt electrode was used as the counter electrode, and a photocatalyst-coated ITO conductive glass was used as the working electrode. The preparation process was to first mix the catalyst and ethanol solution. The mixed system was ground for 15 min, then a proper amount of supernatant was added to ethanol and diluted for 5 min to uniformity, spin-coated on ITO glass, and dried at 60 °C. The light source was a 350 W xenon lamp ( $\lambda \geq 400$  nm), and the electrolyte solution was 0.1 mol/L of Na<sub>2</sub>SO<sub>4</sub> solution. A short photocurrent density measurement was performed during the ON/OFF cycle at 0 V for 450 s. The frequency range test of electrochemical impedance was 100 kW–0.01 W.

### 3.6. Characterization

XRD was measured using an X-ray diffractometer, and CuK $\alpha$  radiation ( $\lambda = 1.5418$  Å) was performed in the range of  $2\theta = 10$ – $80^\circ$ . The scanning electron microscopy (SEM) was performed with a JEOL-1600 field emission microscope with an acceleration voltage of 5 kV. Transmission electron microscopy (TEM) was performed with a JEOL-2100 (Japan JEOL) operating at 200 kV. X-ray photoelectron spectroscopy (XPS) was performed with an ESCALab MKII spectrometer with MgK $\alpha$  radiation, and its binding energy position was calibrated as C 1 s = 284.6 eV. The UV–vis DRS spectra of Bi<sub>2</sub>WO<sub>6</sub>, ZnTiO<sub>3</sub>, and Bi<sub>2</sub>WO<sub>6</sub>/ZnTiO<sub>3</sub> were recorded with an ultraviolet–visible spectrophotometer (UV 2600).

## 4. Conclusions

1. In this paper, 2D/2D heterojunctions of ZnTiO<sub>3</sub> nanosheets/Bi<sub>2</sub>WO<sub>6</sub> nanosheets were prepared for the first time by combining a hydrothermal method and a two-step calcination method, and two types of phenolic pollutants were selected. The effects of photocatalysts on electron-absorbing and electron-donating phenolic pollutants were discussed. It was confirmed that the photocatalyst had an obvious degradation effect on the electron-donating phenolic pollutants. This was because the electron-donating group could accelerate the oxidation of the ortho hydroxyl, making the benzene ring easier to decompose.
2. Compared with pure Bi<sub>2</sub>WO<sub>6</sub> (25%), the degradation rate of phenol by the ZnTiO<sub>3</sub>/Bi<sub>2</sub>WO<sub>6</sub> photocatalyst could reach 93%, and the kinetic rate was increased by 3.6 times. The main reasons for the performance improvement were as follows: (1) 2D/2D ZnTiO<sub>3</sub>/Bi<sub>2</sub>WO<sub>6</sub> heterojunction shortened the charge-transfer path and reduced the resistance of photogenerated electrons and holes to the surface; (2) the S-scheme heterojunction mechanism was constructed at the ZnTiO<sub>3</sub>/Bi<sub>2</sub>WO<sub>6</sub> interface, which maintained a higher oxidation potential and reduction potential and realized the spatial separation of photogenerated carriers; and (3) the photoelectric coupling effect of the applied electric field further promoted the separation of the photogenerated carrier and improved the active free radical  $\cdot\text{OH}$  and  $\cdot\text{O}_2^-$ . This work provides a new strategy for the degradation of phenolic wastewater.

**Author Contributions:** C.Z.: Conceptualization, Methodology, Software, Investigation, Writing—original draft; X.T.: Writing—review and editing; Z.J.: Supervision, Data curation; M.L.: Methodology, Validation, Formal analysis, Visualization; J.J.: Supervision, Data curation, Funding, acquisition; Supervision; Q.S.: Methodology, Validation, Formal analysis, Visualization; X.Y.: Supervision, Data curation. All authors have read and agreed to the published version of the manuscript.

**Funding:** Support for carrying out this work was provided by Shandong Provincial Natural Science (ZR2021QB214) and the Doctoral Research Foundation of Weifang University (2022BS13 and 2021BS48).

**Institutional Review Board Statement:** Not applicable.

**Informed Consent Statement:** Not applicable.

**Data Availability Statement:** Not applicable.

**Conflicts of Interest:** The authors declare no conflict of interest.

## References

1. Antony, R.P.; Mathews, T. Kinetics of dye destruction using electrochemically synthesized sunlight active N-doped and C and N Co-doped TiO<sub>2</sub> nanotubular photocatalysts, *Energy Environ. Focus* **2013**, *2*, 139–148.
2. Ochiai, T.; Fujishima, A. Photoelectrochemical properties of TiO<sub>2</sub> photocatalyst and its applications for environmental purification. *J. Photochem. Photobiol. C* **2012**, *13*, 247–262. [[CrossRef](#)]
3. Zhang, H.; Lv, X. P25-Graphene Composite as a High Performance Photocatalyst. *ACS Nano* **2010**, *4*, 380–386. [[CrossRef](#)]
4. Zhou, W.; Fu, H. ChemInform Abstract: Mesoporous TiO<sub>2</sub>: Preparation, Doping, and as a Composite for Photocatalysis. *ChemCatChem* **2013**, *5*, 885–894. [[CrossRef](#)]
5. Hou, Y.; Li, X. Photoelectrocatalytic activity of a Cu<sub>2</sub>O loaded self-organized highly oriented TiO<sub>2</sub> nanotube array electrode for 4-chlorophenol degradation. *Environ. Sci. Technol.* **2009**, *43*, 858–863. [[CrossRef](#)]
6. Chen, X.; Liu, L.; Yu, P.Y.; Mao, S.S. Increasing Solar Absorption for Photocatalysis with Black Hydrogenated Titanium Dioxide Nanocrystals. *Science* **2011**, *331*, 746–750. [[CrossRef](#)]
7. Luo, J.M.; Dong, G.; Zhu, Y. Switching of semiconducting behavior from n-type to p-type induced high photocatalytic NO removal activity in g-C<sub>3</sub>N<sub>4</sub>. *Appl. Catal. B Environ.* **2017**, *214*, 46–56. [[CrossRef](#)]
8. Deng, F.; Zhang, Q.; Yang, L. Visible-light-responsive graphene-functionalized Bi-bridge Z-scheme black BiOCl/Bi<sub>2</sub>O<sub>3</sub> heterojunction with oxygen vacancy and multiple charge transfer channels for efficient photocatalytic degradation of 2-nitrophenol and industrial wastewater treatment. *Appl. Catal. B Environ.* **2018**, *238*, 61–69. [[CrossRef](#)]
9. Tada, H.; Mitsui, T.; Kiyonaga, T.; Akita, T.; Tanaka, K. All-solid-state Z-scheme in CdS-Au-TiO<sub>2</sub> three-component nanojunction system. *Nat. Mater.* **2006**, *5*, 782–786. [[CrossRef](#)]
10. Zhu, Y.; Xu, D.; Meng, M. Ultrasonic-assisted synthesis of amorphous Bi<sub>2</sub>S<sub>3</sub> coupled (BiO)<sub>2</sub>CO<sub>3</sub> catalyst with improved visible light-responsive photocatalytic activity. *J. Mater. Sci.* **2015**, *50*, 1594–1604. [[CrossRef](#)]
11. Meng, X.C.; Li, Z.Z.; Zeng, H.M.; Chen, J.; Zhang, Z.S. MoS<sub>2</sub> quantum dots-interspersed Bi<sub>2</sub>WO<sub>6</sub> heterostructures for visible light-induced detoxification and disinfection. *Appl. Catal. B Environ.* **2017**, *210*, 160–172. [[CrossRef](#)]
12. Fu, J.W.; Xu, Q.L.; Low, J.X. Ultrathin 2D/2D WO<sub>3</sub>/g-C<sub>3</sub>N<sub>4</sub> step-scheme H<sub>2</sub>-production photocatalyst. *Appl. Catal. B Environ.* **2019**, *243*, 556–565. [[CrossRef](#)]
13. Bao, Y.J.; Song, S.Q.; Yao, G.J. S-Scheme Photocatalytic Systems. *Sol. RRL* **2021**, *5*, 2100118. [[CrossRef](#)]
14. Zhang, L.Y.; Zhang, J.J.; Yu, H.G. Emerging S-Scheme Photocatalyst. *Adv. Mater.* **2022**, *34*, 2107668. [[CrossRef](#)] [[PubMed](#)]
15. Xu, Q.L.; Zhang, L.Y.; Cheng, B. S-Scheme Heterojunction Photocatalyst. *Chem* **2020**, *6*, 1543–1559. [[CrossRef](#)]
16. Wang, J.; Wang, G.H.; Cheng, B. Sulfur-doped g-C<sub>3</sub>N<sub>4</sub>/TiO<sub>2</sub> S-scheme heterojunction photocatalyst for Congo Red photodegradation. *Chin. J. Catal.* **2021**, *42*, 56–68. [[CrossRef](#)]
17. Chen, R.F.; Zhou, W.; Qu, W.W.; Wang, Y.J. A novel hierarchical nanostructured S-scheme RGO/Bi<sub>2</sub>MoO<sub>6</sub>/Bi<sub>2</sub>WO<sub>6</sub> heterojunction: Excellent photocatalytic degradation activity for pollutants. *Appl. Surf. Sci.* **2022**, *588*, 152788. [[CrossRef](#)]
18. Tang, D.Y.; Xu, D.S.; Luo, Z.P. Highly Dispersion Cu<sub>2</sub>O QDs Decorated Bi<sub>2</sub>WO<sub>6</sub> S-Scheme Heterojunction for Enhanced Photocatalytic Water Oxidation. *Nanomaterials* **2022**, *12*, 2455. [[CrossRef](#)] [[PubMed](#)]
19. Li, Y.F.; Xia, Z.L.; Yang, Q. Review on g-C<sub>3</sub>N<sub>4</sub>-based S-scheme heterojunction photocatalysts. *J. Mater. Sci. Technol.* **2022**, *125*, 128–144. [[CrossRef](#)]
20. Han, X.X.; Lu, B.J.; Huang, X. Novel p- and n-type S-scheme heterojunction photocatalyst for boosted CO<sub>2</sub> photoreduction activity. *Appl. Catal. B Environ.* **2022**, *316*, 121587. [[CrossRef](#)]
21. Reddy, K.H.; Martha, S.; Parida, K.M. Erratic charge transfer dynamics of Au/ZnTiO<sub>3</sub> nanocomposites under UV and visible light irradiation and their related photocatalytic activities. *Nanoscale* **2018**, *10*, 18540–18554. [[CrossRef](#)] [[PubMed](#)]
22. Anwer, H.; Mahmood, A.; Lee, J. Photocatalysts for degradation of dyes in industrial effluents: Opportunities and challenges. *Nano Res.* **2019**, *12*, 955–972. [[CrossRef](#)]
23. Chen, F.; Yu, C.; Wei, L. Fabrication and characterization of ZnTiO<sub>3</sub>/Zn<sub>2</sub>Ti<sub>3</sub>O<sub>8</sub>/ZnO ternary photocatalyst for synergetic removal of aqueous organic pollutants and Cr(VI) ions. *Sci. Total Environ.* **2019**, *706*, 136026. [[CrossRef](#)] [[PubMed](#)]
24. Lu, J.; Li, D.; Chai, Y. Rational design and preparation of nanoheterostructures based on zinc titanate for solar-driven photocatalytic conversion of CO<sub>2</sub> to valuable fuels. *Appl. Catal. B-Environ.* **2019**, *5*, 117800. [[CrossRef](#)]
25. Yu, C.; Chen, F.; Zhou, W. A facile phase transformation strategy for fabrication of novel Z-scheme ternary heterojunctions with efficient photocatalytic properties. *Nanoscale* **2019**, *11*, 7720–7733. [[CrossRef](#)] [[PubMed](#)]
26. Huang, J.; Tan, G.; Yang, W. Synthesis and Photocatalytic Properties of N/Bi<sub>2</sub>WO<sub>6</sub> Flower-like Crystallites Self-Assembled from Nanofflakes. *J. Clust. Sci.* **2013**, *24*, 1139–1149. [[CrossRef](#)]
27. Chi, Y.; Yuan, Q.; Hou, S.; Zhao, Z. Synthesis and characterization of mesoporous ZnTiO<sub>3</sub> rods via a polyvinylpyrrolidone assisted sol-gel method. *Ceram. Int.* **2016**, *42*, 5094–5099. [[CrossRef](#)]
28. Meng, X.C.; Zhang, Z.S. Synthesis and characterization of plasmonic and magnetically separable Ag/AgCl-Bi<sub>2</sub>WO<sub>6</sub>@Fe<sub>3</sub>O<sub>4</sub>@SiO<sub>2</sub> core-shell composites for visible light-induced water detoxification. *J. Colloid Interface Sci.* **2017**, *485*, 296–307. [[CrossRef](#)] [[PubMed](#)]

29. Raveendra, R.S.; Prashantha, P.A.; Krishnac, R.H. Synthesis, structural characterization of nano ZnTiO<sub>3</sub> ceramic: An effective azo dye adsorbent and antibacterial agent. *J. Asian Ceram. Soc.* **2014**, *2*, 357–365. [[CrossRef](#)]
30. Hu, J.; Chen, D.; Mo, Z. Z-Scheme 2D/2D Heterojunction of Black Phosphorus/ Monolayer Bi<sub>2</sub>WO<sub>6</sub> Nanosheets with Enhanced Photocatalytic Activities. *Angew. Chem. Int. Ed.* **2019**, *58*, 2073–2077. [[CrossRef](#)]
31. Xu, J.; Yue, J.; Niu, J. Fabrication of Bi<sub>2</sub>WO<sub>6</sub> quantum dots/ultrathin nanosheets 0D/2D homojunctions with enhanced photocatalytic activity under visible light irradiation. *Chin. J. Catal.* **2018**, *39*, 1910–1918. [[CrossRef](#)]
32. Zhu, Z.L.; Ren, Y.; Li, Q. One-pot electrodeposition synthesis of Bi<sub>2</sub>WO<sub>6</sub>/graphene composites for photocatalytic applications under visible light irradiation. *Ceram. Int.* **2018**, *44*, 3511–3516. [[CrossRef](#)]
33. Wang, R.S.; Li, B.; Xiao, Y. Optimizing Pd and Au-Pd decorated Bi<sub>2</sub>WO<sub>6</sub> ultrathin nanosheets for photocatalytic selective oxidation of aromatic alcohols. *J. Catal.* **2018**, *364*, 154–165. [[CrossRef](#)]
34. He, W.; Sun, Y.; Jiang, G. Activation of amorphous Bi<sub>2</sub>WO<sub>6</sub> with synchronous Bi metal and Bi<sub>2</sub>O<sub>3</sub> coupling: Photocatalysis mechanism and reaction pathway. *Appl. Catal. B Environ.* **2018**, *232*, 340–347. [[CrossRef](#)]
35. Ranjith, K.S.; Uyar, T. Conscientious Design of Zn-S/Ti N Layer by Transformation of ZnTiO<sub>3</sub> on Electrospun ZnTiO<sub>3</sub>@TiO<sub>2</sub> Nanofibers: Stability and Reusable Photocatalytic Performance under Visible Irradiation. *ACS Sustain. Chem. Eng.* **2018**, *6*, 12980–12992. [[CrossRef](#)]
36. Qian, W.; Greaney, P. Low-Temperature Nitrogen Doping in Ammonia Solution for Production of N-Doped TiO<sub>2</sub>-Hybridized Graphene as a Highly Efficient Photocatalyst for Water Treatment. *ACS Sustain. Chem. Eng.* **2014**, *2*, 1802–1810. [[CrossRef](#)]
37. Long, G.Y.; Ding, G.Y. Fabrication of mediator-free g-C<sub>3</sub>N<sub>4</sub>/Bi<sub>2</sub>WO<sub>6</sub> Z-scheme with enhanced photocatalytic reduction dechlorination performance of 2,4-DCP. *Appl. Surf. Sci.* **2018**, *455*, 1010–1018. [[CrossRef](#)]
38. Zhang, Z.; Shen, Q.H.; Cissoko, N. Catalytic dechlorination of 2,4-dichlorophenol by Pd/Fe bimetallic nanoparticles in the presence of humic acid. *J. Hazard. Mater.* **2010**, *182*, 252–258. [[CrossRef](#)] [[PubMed](#)]
39. Arellano-Gonzalez, M.A.; Texier, A.C.; Lartundo-Rojas, L.; Gonzalez, I. Electrochemical dechlorination of 2-chlorophenol on Pd/Ti, Ni/Ti and Pd-Ni Alloy/Ti electrodes. *J. Electrochem. Soc.* **2015**, *162*, 223–230. [[CrossRef](#)]
40. Gawande, S.B.; Gawande, K.B.; Thakare, S.R. Photocatalytic degradation of phenol over novel rod shaped graphene@BiPO<sub>4</sub> nanocomposite. *J. Phys. Chem. Solids* **2015**, *85*, 132–137. [[CrossRef](#)]
41. Yu, X.; Wang, L.; Feng, L.J. Preparation of Au/BiOBr/Graphene composite and its photocatalytic performance in phenol degradation under visible light. *J. Fuel. Chem. Tech.* **2016**, *44*, 937–942. [[CrossRef](#)]
42. Wang, L.; Wang, X.; Yin, J. Silica induced oxygen vacancies in supported mixed-phase TiO<sub>2</sub> for photocatalytic degradation of phenol under visible light irradiation. *Catal. Commun.* **2016**, *87*, 98–101. [[CrossRef](#)]
43. Shandilya, P.; Mittal, D.; Soni, M. Fabrication of fluorine doped graphene and SmVO<sub>4</sub> based dispersed and adsorptive photocatalyst for abatement of phenolic compounds from water and bacterial disinfection. *J. Clean Prod.* **2018**, *203*, 386–399. [[CrossRef](#)]
44. Qi, F.; An, W.J.; Wang, H. Combing oxygen vacancies on TiO<sub>2</sub> nanorod arrays with g-C<sub>3</sub>N<sub>4</sub> nanosheets for enhancing photoelectrochemical degradation of phenol. *Mater. Sci. Semicond. Process* **2020**, *109*, 104954. [[CrossRef](#)]
45. Baishnisha, A.; Divakaran, K.; Balakumar, V. Synthesis of highly efficient g-CN@CuO nanocomposite for photocatalytic degradation of phenol under visible light. *J. Alloy Compd.* **2021**, *886*, 161167. [[CrossRef](#)]
46. Chen, W.; Liu, T.Y.; Huang, T. In situ fabrication of novel Z-scheme Bi<sub>2</sub>WO<sub>6</sub> quantum dots/g-C<sub>3</sub>N<sub>4</sub> ultrathin nanosheets heterostructures with improved photocatalytic activity. *Appl. Surf. Sci.* **2015**, *355*, 379–387. [[CrossRef](#)]
47. Jiang, D.L.; Wan, X. Enhanced photocatalytic activity of graphitic carbon nitride/carbon nanotube/Bi<sub>2</sub>WO<sub>6</sub> ternary Z-scheme heterojunction with carbon nanotube as efficient electron mediator. *J. Colloid Interface Sci.* **2018**, *512*, 693–700. [[CrossRef](#)]
48. Guo, H.P.; Hayakawa, T.; Nogami, M.; Hao, Z. Zinc titanium glycolate acetate hydrate and its transformation to zinc titanate microrods: Synthesis, characterization and photocatalytic properties. *Rsc Adv.* **2015**, *5*, 88590–88601.
49. Li, X.B.; Xiong, J.; Huang, J.T. Novel g-C<sub>3</sub>N<sub>4</sub>/h' ZnTiO<sub>3</sub>-a' TiO<sub>2</sub> direct Z-scheme heterojunction with significantly enhanced visible-light photocatalytic activity. *J. Alloy. Compd.* **2019**, *774*, 768–778. [[CrossRef](#)]
50. Ruan, X.; Hu, Y.Y. Effectively enhanced photodegradation of Bisphenol A by in-situ g-C<sub>3</sub>N<sub>4</sub>-Zn/Bi<sub>2</sub>WO<sub>6</sub> heterojunctions and mechanism study. *Chemosphere* **2020**, *246*, 125782. [[CrossRef](#)] [[PubMed](#)]
51. Li, B.R.; Cui, Y.H.; Feng, Y. Study of enhanced photocatalytic performance mechanisms towards a new binary-Bi heterojunction with spontaneously formed interfacial defects. *Appl. Surf. Sci.* **2020**, *532*, 147412. [[CrossRef](#)]

**Disclaimer/Publisher's Note:** The statements, opinions and data contained in all publications are solely those of the individual author(s) and contributor(s) and not of MDPI and/or the editor(s). MDPI and/or the editor(s) disclaim responsibility for any injury to people or property resulting from any ideas, methods, instructions or products referred to in the content.